nature communications

Article

https://doi.org/10.1038/s41467-025-65194-0

Enhancing the ORR durability of single atomic Fe-N_4 active sites with implanted SiO_2 nanoparticles as radical and H_2O_2 inhibitors

Received: 10 October 2024

Accepted: 8 October 2025

Published online: 19 November 2025

Check for updates

Maosong Liu[1], Zhihao Lei[2], Xianhe Lv[1], Xiaoxue Song[1], Long Zhang[1], Shun Li[1], Tao Sun[1], Li Li[1], Jianing Hui[3], Wenyong Zhang[3], Siew Yee Wong[4], Xu Li[4,5] ✉, Guang-Jie Xia[6] ✉, Jianming Zhang[1,4] ✉ & Shuhui Sun[7] ✉

Highly efficient and durable single-atom catalysts (SACs) hold great promise for improving oxygen reduction reaction (ORR) in metal-air batteries and fuel cells. However, their long-term stability is challenged by the byproducts such as H_2O_2 and undesirable radicals. Herein, we report a Fe-N_4 active center-based SAC decorated with SiO_2 nanoparticles (NPs) as a radical scavenger, which was prepared using coffee grounds and industrial spent acid residue. The presence of SiO_2 NPs effectively suppresses the electrochemical H_2O_2 production, significantly improving durability with only a 5 mV half-wave potential loss after 30,000 voltage cycles in alkaline media. Electrochemical evaluations, in-situ characterizations, and density functional theory calculations reveal that the Fe-O-Si binding at the SiO_2–Fe-N_4 interface strengthens the binding of OOH* species, facilitating the 4-electron selectivity in ORR while inhibiting the formation of H_2O_2 and reactive oxygen species. Additionally, the SiO_2 NPs prevent the aggregation of Fe single atomic sites, thereby stabilizing the SAC active sites. Therefore, the incorporation of SiO_2 NP into Fe-based SAC offers a straightforward and effective strategy for enhancing ORR performance.

The development of highly durable electrocatalysts for oxygen reduction reaction (ORR) is crucial for advancing fuel cells and metal-air batteries[1–4]. Platinum-group metal-free (PGM-free) catalysts, recognized for their cost-effectiveness and abundant availability, have emerged as promising alternatives to Pt-based materials[5–7]. Amongst single-atom catalysts (SACs), featuring transition metal-nitrogen coordination moieties on carbon materials (MNC, M = Fe, Co, Cu, etc.), have shown promising activity[8–11]. However, their practical application remains hindered by insufficient catalytic stability, as active sites undergo deactivation and degradation under harsh operating conditions, such as high potentials and acidic environments[12–14]. Recent advances argued that the ORR performance decline may stem from N-group protonation, demetallation, and electrochemical carbon corrosion[15–19].

In Fe–N–C SACs, one of the most extensively studied models, the high ORR activity originates from the dense, O_2-accessible Fe–N_x active sites. However, this is counterbalanced by poor stability due to the generation of reactive oxygen species (ROS), such as •OH and HO_2•, in close proximity to Fe–N_x moieties. These ROS can oxidize the carbon support to CO_2, leading to the demetallation of active metal centers

[1]School of Chemistry and Chemical Engineering, Jiangsu University, Zhenjiang, China. [2]Global Innovative Center of Advanced Nanomaterials, College of Engineering, Science and Environment, University of Newcastle, Callaghan, NSW, Australia. [3]Jiangsu Cnano Technology Co., Ltd, New District, Zhenjiang, China. [4]Institute of Materials Research and Engineering (IMRE), Agency for Science, Technology and Research (A*STAR), 2 Fusionopolis Way, Innovis #08-03, 138634 Singapore, Singapore. [5]Institute of Sustainability for Chemicals, Energy and Environment (ISCE2), Agency for Science, Technology and Research (A*STAR), 1 Pesek Road Jurong Island, 627833 Singapore, Singapore. [6]School of Physical Sciences, Great Bay University & Great Bay Institute for Advanced Study, Dongguan, China. [7]Institut National de la Recherche Scientifique (INRS), Centre Énergie Matériaux Télécommunications, Québec, Canada. ✉e-mail: LI_Xu@a-star.edu.sg; xiagj@gbu.edu.cn; zhangjm@ujs.edu.cn; shuhui.sun@inrs.ca

https://doi.org/10.1038/s41467-025-65194-0

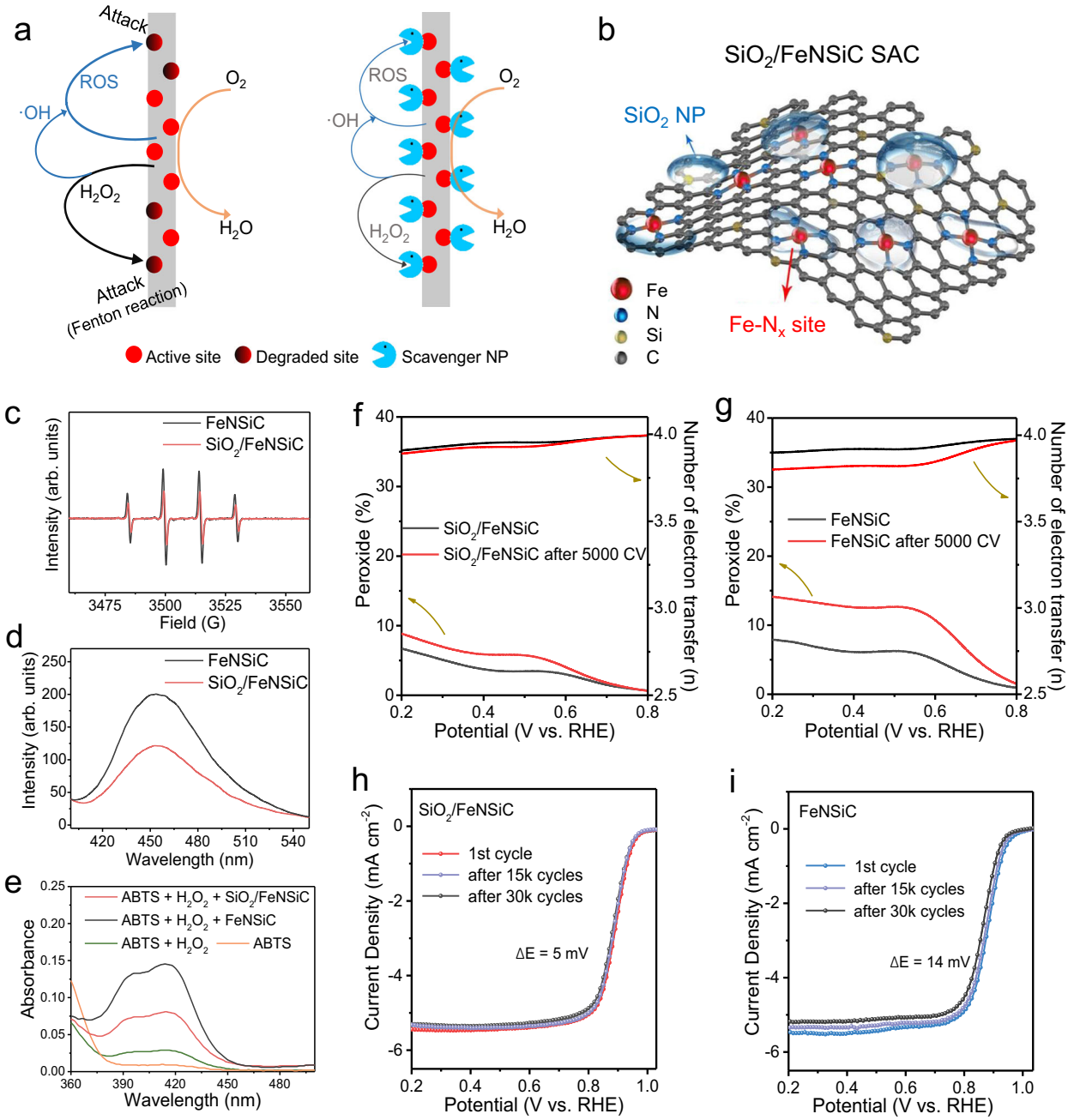

Fig. 1 | The ORR pathway of proposed structure, radicals characterization, and stability measurements with and without scavengers. a Schematic illustrations of ORR pathway over FeNC SAC with and without scavengers and (**b**) the proposed structure of SiO_2/FeNSiC SAC. **c** EPR spectra of the OH–DMPO• radical and (**d**) PL intensity of 7-hydroxycoumarins in the electrochemical measurement of SiO_2/FeNSiC and FeNSiC. **e** UV–Vis spectral variations of ABTS• + radical monitored under various conditions. H_2O_2 yield and n after 1 and 5,000 potential cycles of SiO_2/FeNSiC (**f**) and FeNSiC (**g**). ORR polarization curves before and after 30,000 potential cycles (0.6–1.0 V vs. RHE) in O_2-saturated 0.1 M KOH of (**h**) SiO_2/FeNSiC and (**i**) FeNSiC without iR-corrected. Source data are provided as a Source Data file.

(Fig. 1a, left)[15,20,21]. Additionally, accumulated H_2O_2 further exacerbates degradation by producing highly reactive •OH radicals through Fenton-like reactions at Fe–N_x sites[22,23]. Also, high local concentrations of H_2O_2 can promote carbon oxidation and Fe–N bond cleavage, further compromising stability[24,25]. Therefore, mitigating ROS and H_2O_2 generation is essential for enhancing the durability of Fe–N–C SACs.

To tackle the issues of FeNC SACs stability, passive shielding strategy focused on increasing carbon substrate graphitization to improve resistance against H_2O_2-induced damage, albeit often at the cost of Fe–N_x site density[26,27]. Very recently, a proactive approach has gained traction, emphasizing the direct elimination of ROS and H_2O_2 to enhance Fe–N–C SAC viability in ORR (Fig. 1a, right). For example, Hu et al. incorporated Ta-TiO_x nanoparticles (NPs) as radical scavengers, significantly improving Fe–N–C SAC durability through suppression of H_2O_2 accumulation and fast decomposition of ROS via homolytic O–O bond cleavage at TaO_2–OH surfaces[28]; Moreover, Other studies have also shown that CeO_2 NPs improve SAC robustness by leveraging the Ce^{3+}/Ce^{4+} redox couple and oxygen vacancies to neutralize ROS and buffer oxidative stress[29–33]. These oxides not only scavenge radicals but also modulate the local electronic environment, suppressing Fe demetalation and Fenton-type degradation through interfacial charge redistribution and interfacial bonding.

In this regime, efficient radical scavenging relies on the uniform dispersion and size control of the oxide NP scavengers; small-sized NPs, uniformly distributed in proximity to the Fe–N_4 center, can efficiently neutralize the free radicals[29,34]. Thus, constructing scavenger NP–Fe–N_4 junctions in SACs via a robust manner, to efficiently suppress radicals, is highly desirable and appealing. Silica (SiO_2), bearing high stability and inertness, has been widely employed as a hard template or protective shield material against metal atom agglomeration in SAC fabrication[35–37]. Typically, the SiO_2 is often removed by hydrofluoric acid (HF) etching to increase SAC porosity and active site exposure. Despite its well-established role in SAC fabrication, the potential influence of SiO_2 on M-N_x active moieties has, to our knowledge, been largely overlooked.

In this work, we demonstrate the previously unrecognized function of SiO_2 in enhancing Fe–N–C SAC stability by acting as a radical scavenger and H_2O_2 inhibitor in ORR. Inspired by the fact that Si is distributed uniformly throughout plant tissues mainly as a hydrated amorphous SiO_2 polymers[38–40], a simple hydrolysis process, utilizing biomass of coffee grounds (CGs) and industrial spent acid (ISA), was designed to produce SiO_2 NP-modified Fe–N–Si–C SAC (SiO_2/FeNSiC). The SiO_2 NPs, naturally formed from CG decomposition, were uniformly distributed along the carbon scaffold, ensuring proximity to the active sites. Electrochemical evaluations, dynamic in situ characterizations, and density functional theory (DFT) calculations collectively suggest that embedded SiO_2 NPs play a crucial role in suppressing H_2O_2 and radical generation during ORR.

Results and discussion

Catalyst fabrication and characterization

The Coffee grounds (CGs) primarily consist of cellulose, lignin, and hemicellulose, along with a small proportion of Si content (~3.66 wt%, as determined by inductively-coupled-plasma-optical-emission spectrometry (ICP-OES)). Given their natural abundance, sustainability, and cost-effectiveness, CGs serve as both carbon and silicon sources for SAC synthesis. Thanks to the homogeneous distribution of Si-containing substances in the tissue, small-sized SiO_2 NPs can be in situ formed and evenly dispersed in the carbon matrix upon the carbonization of CGs. Another precursor ISA (Supplementary Table 1), derived from the industrial steel cleaning process, is mainly comprised of hydrochloric acid (HCl) and $FeCl_3$. Our previous study has verified that the $FeCl_3$ in ISA, acting as Lewis acid, can favor the formation of nanopores within the carbon matrix, with Fe^{3+} ions embedded inside[41]. The noticeable porosity differences between CGs treated with and without ISA were visible through scanning electron microscopy (SEM) observation (Supplementary Fig. 1). Following ISA treatment, the CGs underwent pyrolysis in the presence of urea as a nitrogen source, yielding the final SiO_2/FeNSiC SAC (see schematic structure in Fig. 1b). To elucidate the role of SiO_2 in catalysis, FeNSiC (without SiO_2) and FeNC (lacking both SiO_2 and Si atoms) were also prepared for comparative study (see Materials Section for their synthesis).

To assess the •OH scavenging capability of the as-prepared catalysts with and without SiO_2, electron paramagnetic resonance (EPR) spin trapping experiments were conducted using 5,5-dimethyl-1-pyrroline N-oxide (DMPO) as a trapping agent through a Fenton reaction. As displayed in Fig. 1c, the EPR peak intensity is notably suppressed for SiO_2/FeNSiC compared to FeNSiC, indicating enhanced radical scavenging. Additionally, fluorescence-based •OH detection using a coumarin molecular probe revealed a lower photoluminescence (PL) intensity for 7-hydroxycoumarin in the presence of SiO_2/FeNSiC, further confirming its •OH scavenging function (Fig. 1d)[28]. To evaluate ROS scavenging efficiency, ultraviolet-visible (UV-vis) spectroscopy was performed using 2,2′-azino-bis (3-ethylbenzothiazoline-6-sulfonic acid) diammonium salt (ABTS) as a probe. The SiO_2/FeNSiC catalyst exhibited a significantly lower absorbance at ~417 nm compared to FeNSiC, suggesting enhanced ROS elimination, possibly due to improved surface properties or catalytic activity (Fig. 1e)[42]. The impact of SiO_2 on H_2O_2 selectivity during ORR was further investigated using rotating ring-disk electrode (RRDE) measurements. As illustrated in Fig. 1f of the electron transfer number (n) and H_2O_2 yield before and after 5000 cyclic voltammetry (CV) manner, respectively, the H_2O_2 yield of the SiO_2/FeNSiC remained at a low level during 1 and 5000 potential cycles, with only a small increase from 6.7 to 8.8% at 0.2 V vs. RHE after cycling; meanwhile, the n after cycling is still retained at ~4, implying a good 4-electron transfer pathway during ORR. By stark contrast, the H_2O_2 yield over FeNSiC without SiO_2 is increased to ~14.1% from 7.9% of the initial value (Fig. 1g). Further continuous CV process for 30,000 cycles in an O_2-saturated KOH solution (0.1 M) between 0.6 V and 1.0 V showed the highest durability for SiO_2/FeNSiC after cycling, with a half-wave potential ($E_{1/2}$) loss of only 5 mV, much smaller than that of FeNSiC (14 mV), FeNC (18 mV) and Pt/C (28 mV after 5000 cycles) (Fig. 1h, i, Supplementary Fig. 2). The reduced H_2O_2 formation in the SiO_2/FeNSiC system likely contributes to its enhanced durability; notably, Si doping alone was insufficient to improve FeNC stability. Similar trends were observed under acidic conditions (Supplementary Fig. 3), where SiO_2-containing samples exhibited lower $E_{1/2}$ degradation (32 mV vs. 70 mV) and reduced H_2O_2 yield (5.0% to 8.9% vs. 7.9% to 15.3% at 0.2 V) after 5000 CV cycles, further validating the stabilizing role of SiO_2.

The structural traits of the SiO_2/FeNSiC were meticulously characterized. As depicted in Fig. 2a, b of the transmission electron microscopy (TEM) images, the sample exhibits a layered architecture interspersed with darker particles ranging from 5 to 20 nm in size. The aberration-corrected high-angle annular dark-field scanning TEM (HAADF-STEM) image (Fig. 2d) reveals numerous bright spots, indicative of heavier metal atoms, confirming the atomic dispersion of Fe sites within the structure. Additionally, energy-dispersive spectroscopy (EDS) mapping (Fig. 2e) demonstrates the uniform distribution of Fe, N, Si, O, and C across the carbon substrate. While HAADF-STEM confirms the atomic distribution of Fe, the composition of the darker particles observed in Fig. 2a, b required further identification. To address this, more precise analysis of electron energy-loss spectroscopy (EELS) was employed to detect the characteristic energy-loss edges of the possible key elements of the particles, which provides significantly higher energy resolution and sensitivity than the EDS to light elements (e.g., C, O, Si, etc.). As illustrated in Fig. 2c, the EELS analysis reveals that these darker particles are primarily composed of Si and O, as evidenced by the distinct O K-edge (~532 eV) and Si K-edge (~1850 eV), confirming that these particles are predominantly SiO_2 rather than carbon NPs or overlapping carbon layer fragments. These findings strongly verify that the sample comprises Fe–N–Si–C single-atomic sites accompanied by homogeneously dispersed SiO_2 NPs within the carbon matrix.

The chemical state of the SiO_2/FeNSiC, FeNSiC, and FeNC samples (Supplementary Fig. 4; Supplementary Table 2) was explored using X-ray photoelectron spectroscopy (XPS) measurement. The peaks at ~101 and ~103 eV of the Si 2*p* spectrum indicated by Supplementary Fig. 4a can be assigned to the –C–Si–O– bonds and SiO_2 in the SiO_2/FeNSiC sample, respectively; while the band belonging to the SiO_2 cannot be identified in the FeNSiC sample. The Fe 2*p* spectra (Supplementary Fig. 4b) agree with the coexistence of Fe^{2+} and Fe^{3+} species, with the Fe $2p_{3/2}$ peak in SiO_2/FeNSiC shifting positively by +0.43 eV relative to unmodified Fe–N–C, suggesting electronic interactions between Fe and SiO_2. After deconvolution, the high-resolution spectra of N 1*s* (Supplementary Fig. 4c) reveal four peaks at 403.5, 401.0, 400.2, and 398.4 eV, ascribed to oxidation-N, graphite-N, pyrrole-N, and pyridine-N, respectively[43,44]. The C 1s spectra (Supplementary Fig. 4d) show the primary chemical bonds of C–C, C–N, C–O, C = O, and C–Si in both the SiO_2/FeNSiC and FeNSiC samples, confirming the presence of Si species[45].

https://doi.org/10.1038/s41467-025-65194-0

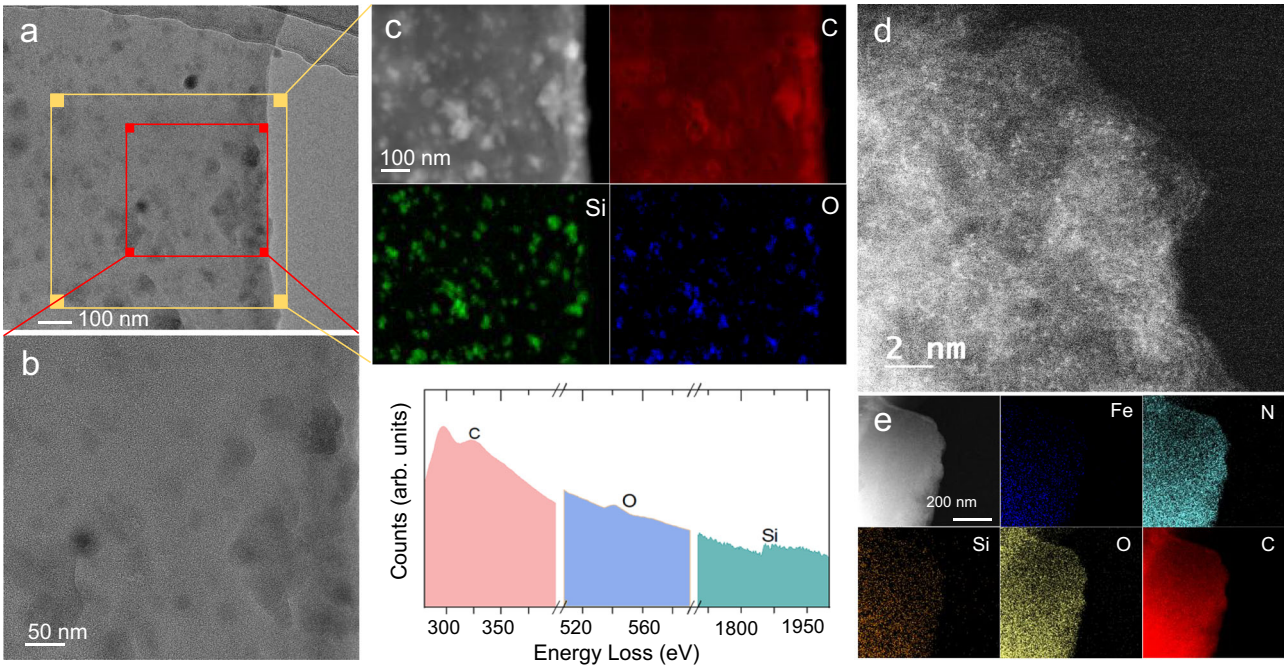

Fig. 2 | Structural characterization of the SiO_2/FeNSiC sample. a, b Images of TEM observation and (**c**) corresponding EELS analysis (C: red, Si: green, O: blue). **d** HAADF-STEM images of the SiO_2/FeNSiC (bright spots indicate the single metal atoms). **e** Images of Dark-field TEM observation and corresponding EDS elemental mapping for Fe (blue), N (cyan), Si (orange), O (yellow) and C (red) in the SiO_2/FeNSiC sample. Source data are provided as a Source Data file.

To overcome the low signal-to-noise ratio in XPS Fe 2*p* spectra, ^{57}Fe Mössbauer spectroscopy was employed for precise iron species identification (Supplementary Fig. 5). The spectrum of SiO_2/FeNSiC was resolved into two distinct doublets, corresponding to Fe–N_x coordination environments with Fe(III) existing in both high-spin (D1) and low-spin (D2) states[46]. Raman spectra in Supplementary Fig. 6a present the characteristics of defect (D) and graphite (G) carbon of the samples. The I_D/I_G intensity ratios for all samples were calculated to be ~1.0, implying that the SiO_2 NPs scarcely affect the carbon structure in SiO_2/FeNSiC. Crystallographic analysis via X-ray diffraction (XRD) (Supplementary Fig. 6b) reveals no discernible peaks corresponding to Fe-based compounds, suggesting that Fe exists in a monoatomic state within the carbon matrix—consistent with TEM observations.

To further elucidate the atomic dispersion and local coordination environment of Fe in SiO_2/FeNSiC, we implemented extended X-ray absorption fine structure (EXAFS) and X-ray absorption near-edge structure (XANES) measurements. The Fe K-edge XANES spectra for SiO_2/FeNSiC, FeNSiC, and FeNC, alongside reference samples (Fe_2SiO_4, FeO, Fe_2O_3, Fe foil, and iron phthalocyanine (FePc)), are presented in Fig. 3a. The Fe species in SiO_2/FeNSiC exhibit a higher average oxidation state than metallic Fe and FeO, as indicated by the positive shift in the Fe K-edge absorption energy compared to Fe foil and FeO[47]. Furthermore, the Fe–N coordination at the first shell can be clarified by the Fourier-transform EXAFS (FT-EXAFS) spectrum of the SiO_2/FeNSiC, which manifests one dominant peak at ~1.5 Å, with no Fe–Fe scattering visible at ~2.2 Å (Fig. 3b), effectively excluding the possibility of any Fe agglomerates in the sample[48,49].

The EXAFS results were fitted to investigate the nearby coordination of the Fe center in SiO_2/FeNSiC (Fig. 3c, d; Supplementary Table 3). Combined with ^{57}Fe Mössbauer spectroscopy, the results suggest that Fe atoms in SiO_2/FeNSiC predominantly adopt a Fe–N_4 coordination geometry, characteristic of a classical Fe–N_4 structure[50,51]. Interestingly, a secondary peak appears in the light at a high R value (ca. 2.2 Å) in the SiO_2/FeNSiC sample, indicating an additional definite path that should also be accounted for the surrounding coordination of metal centers. Considering the presence of Si and O elements in this sample, we analyzed the possible connection modes of Fe with O and Si atoms; the fitting outcomes in Supplementary Table 3 indicate no direct coordination between Fe and Si atoms in the outer shell of SiO_2/FeNSiC, as the fitted Fe-Si interatomic distance (2.94 Å) is too large to support direct coordination. Instead, the Fe and Si species likely interact through oxygen bridges, forming Fe–O–Si linkages. This conclusion is further supported by complementary XPS and FTIR analyses (Supplementary Fig. 7). The secondary peak at ~2.03 Å corresponds to Fe-O bonding, with a coordination number of ~1.02, reinforcing the presence of Fe–O–Si motifs in the sample[52,53]. To further probe the local coordination environment, wavelet transform (WT) analysis of Fe K-edge EXAFS was performed (Fig. 3e–h). SiO_2/FeNSiC exhibits a dominant intensity maximum at ~5.0 $Å^{-1}$, characteristic of Fe–N scattering. Importantly, no Fe–Fe scattering signal (~9.0 $Å^{-1}$) is detected, corroborating the absence of Fe aggregates. The WT contour for SiO_2/FeNSiC closely aligns with that of FeNC, indicating a similar Fe–N coordination environment. However, a subtle shift toward the Fe_2O_3 position suggests the presence of Fe–O bonds, further validating the formation of Fe–O–Si linkages in SiO_2/FeNSiC[53,54].

The porosity of all the SAC samples was analyzed using N_2 adsorption/desorption measurement. Supplementary Fig. 8a shows that SiO_2/FeNSiC, FeNSiC, and FeNC samples possess type-I and type-IV nanopore arrangements, with a hysteresis loop at $P/P_0 \approx 0.9$, indicating the presence of a well-developed micro-/mesoporous structure. Supplementary Fig. 8b, c present the pore size distribution and cumulative pore volume, calculated using a detailed quenched solid density functional theory (QSDFT) model. These SACs are predominantly occupied by micropores (<2 nm) and narrow mesopores (2–10 nm). Supplementary Table 4 summarizes the substantial surface area and total pore volume of all samples prepared with and without ISA treatment. Apparently, ISA treatment to CGs results in a significant increase of surface area (~1400–1500 $m^2\ g^{-1}$) by constructing multiple micro-/mesopores, attributed to the important role of Fe^{3+} in ISA as a Lewis acid, which can facilitate the hydrolysis of cellulose chain for pore creation[41,55,56].

https://doi.org/10.1038/s41467-025-65194-0

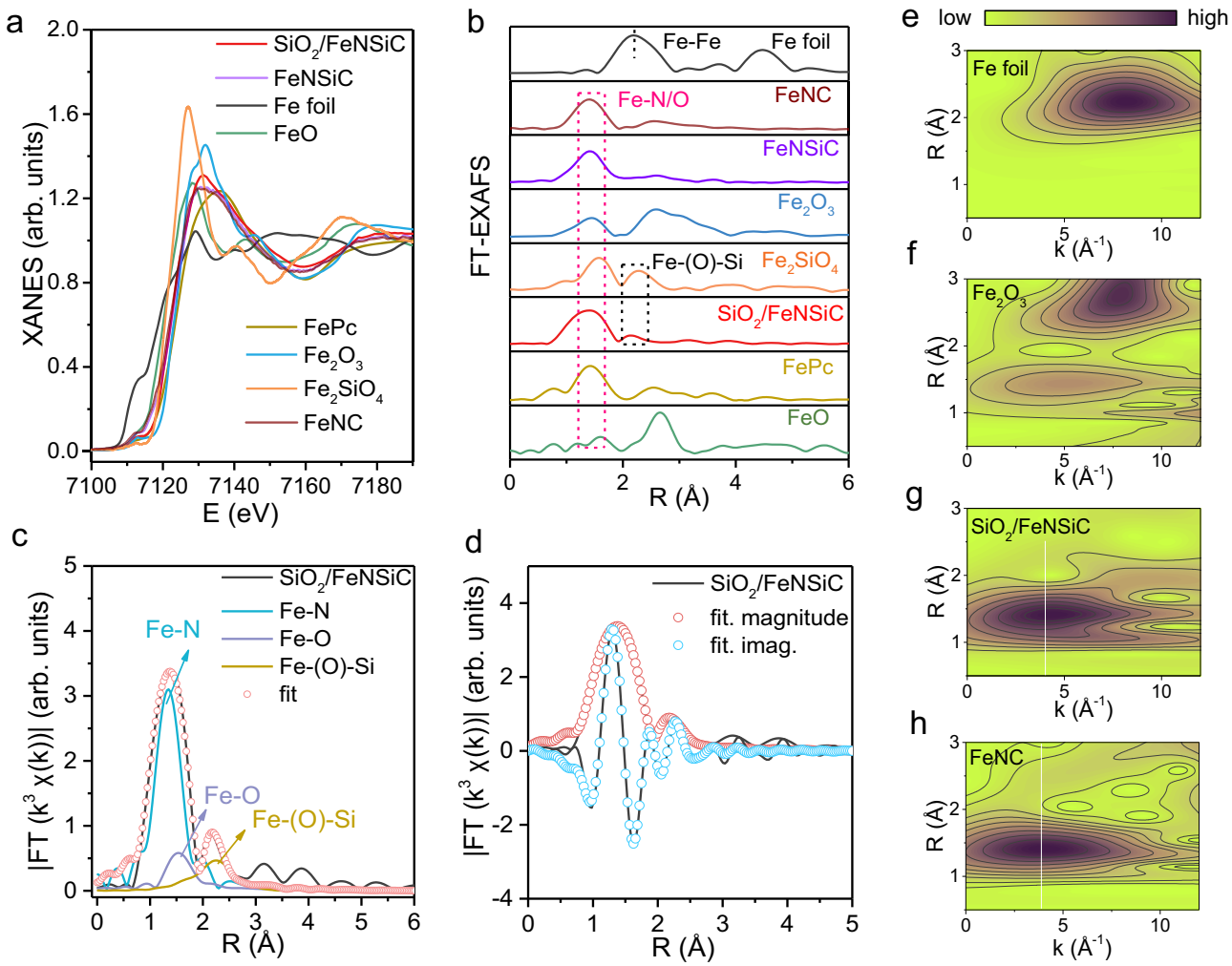

Fig. 3 | X-ray absorption spectroscopy characterization of SiO_2/FeNSiC and other samples. a Fe K-edge X-ray absorption near-edge structure (XANES) and (**b**) Fourier transform k^3-weighted Fe K-edge extended X-ray absorption fine structure (FT-EXAFS) spectra of SiO_2/FeNSiC, FeNSiC, FeNC, Fe_2SiO_4, Fe foil, FeO, Fe_2O_3, and FePc. **c, d** Experimental (black line) and fitted (red cycle) Fe FT-EXAFS fitting signals in R space of SiO_2/FeNSiC (the individual paths indicate unrefined theoretical scattering paths from the fitted FEFF model, indicating their baseline radial positions and qualitative relevance). Wavelet transform (WT)-EXAFS of the Fe K-edge of (**e**) Fe foil, (**f**) Fe_2O_3, (**g**) SiO_2/FeNSiC and (**h**) FeNC from top to bottom. Source data are provided as a Source Data file.

Electrochemical catalytic properties

In subsequent electrochemical catalytic tests, SiO_2/FeNSiC exhibited an $E_{1/2}$ of 0.892 V vs. RHE in linear sweep voltammetry (LSV), surpassing FeNSiC (0.875 V), FeNC (0.877 V), and Pt/C (0.863 V) (Fig. 4a). In addition, SiO_2/FeNSiC showed a high kinetic current density of 21.18 mA cm^{-2} at 0.85 V (J_k, Fig. 4b), outperforming FeNSiC (11.6 mA cm^{-2}), FeNC (16.92 mA cm^{-2}) and Pt/C (7.02 mA cm^{-2}). The favorable ORR kinetics of SiO_2/FeNSiC were evidenced by its low Tafel slope of 60.3 mV dec^{-1} (Fig. 4c), smaller than that of FeNSiC (82.6 mV dec^{-1}), FeNC (62.2 mV dec^{-1}) and Pt/C (78.1 mV dec^{-1}). The H_2O_2 yield detected upon SiO_2/FeNSiC is fairly lower (~6%) than those of FeNSiC (7.9%) and FeNC (10.8%), and comparable to that of Pt/C (~5%) at 0.2 V vs. RHE, as illustrated in Fig. 4d, indicating a favorable 4-electron transfer process. The robustness of the SiO_2/FeNSiC was further confirmed through chronoamperometry (CA) tests at a high potential of 0.75 V vs. RHE. As displayed in Supplementary Fig. 9, the SiO_2/FeNSiC shows only a 7.4% reduction in current after 50,000 s, much better than the Pt/C with a 30% decline, indicating a commendable stability of the SiO_2/FeNSiC. Notably, the incorporation of SiO_2 not only enhances stability but also improves the ORR activity of the SACs. Furthermore, the ORR performance of FeNC-based samples, both with and without SiO_2, along with Pt/C, was evaluated in an O_2-saturated 0.5 M H_2SO_4 electrolyte (Supplementary Fig. 10). The J_k@0.8 V, $E_{1/2}$ and Tafel slope obtained from the LSV curves reveal that SiO_2/FeNSiC exhibits moderate ORR activity (J_k = 1.86 mA cm^{-2}, $E_{1/2}$ = 0.764 V, 77.3 mV dec^{-1}) compared to FeNSiC (J_k = 0.87 mA cm^{-2}, $E_{1/2}$ = 0.712 V, 126.8 mV dec^{-1}). However, despite these improvements, the performance remains inferior to commercial Pt/C (J_k = 9.26 mA cm^{-2}, $E_{1/2}$ = 0.82 V, 79.6 mV dec^{-1}), indicating further optimization is required for practical applications.

To investigate the potential dissolution mechanism of SiO_2 under alkaline conditions (0.1 M KOH), inductively coupled plasma (ICP) analysis was performed to quantify SiO_2 leaching during ORR stability tests (Supplementary Fig. 11). The results confirmed that Si dissolution was negligible. Furthermore, post-stability test characterization using TEM, EELS, and XPS (Supplementary Figs. 12, 13) revealed the continued presence of uniformly dispersed SiO_2 NPs, indicating their structural integrity and sustained functionality as reactive oxygen species (ROS) and H_2O_2 scavengers in 0.1 M KOH. To assess the accessibility of active sites, a critical factor in ORR performance, nitrite poisoning experiments were conducted on FeNC catalysts with and without SiO_2 (Supplementary Fig. 14a, b). CV analysis of the poisoned samples (Supplementary Fig. 14c, d) showed a slightly higher stripping charge for the SiO_2/FeNSiC catalyst compared to its SiO_2-free

https://doi.org/10.1038/s41467-025-65194-0

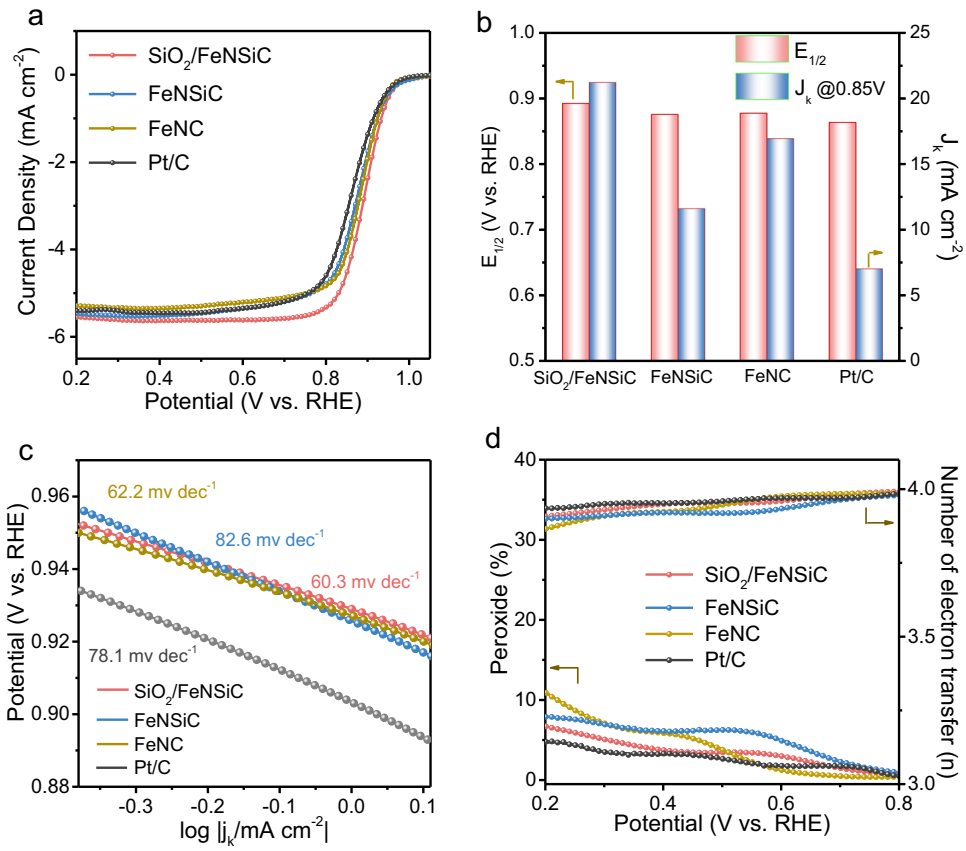

Fig. 4 | Electrochemical tests of SiO_2/FeNSiC and other reference catalysts. **a** ORR polarization curves, (**b**) half-wave potential ($E_{1/2}$) and kinetic current density (J_k) at 0.85 V vs. RHE, (**c**) corresponding Tafel plots, (**d**) peroxide (H_2O_2)% and electron transfer number (n) recorded on SiO_2/FeNSiC, FeNSiC, FeNC, and Pt/C in O_2-saturated 0.1 M KOH at 1600 rpm with scan rate of 5 mV s^{-1} (pH = 13.0 ± 0.2, the resistance of the solution was 45 ± 5 Ω) without iR-corrected. Source data are provided as a Source Data file.

counterpart. The Fe–N_x site density (SD), quantified based on the stripping charge, exhibited comparable values for both catalysts (5.74×10^{19} site g^{-1} vs. 5.13×10^{19} site g^{-1}). This confirms that the Fe–N_x active sites remain fully accessible in the presence of SiO_2, ruling out potential site-blocking effects and underscoring the compatibility of SiO_2 integration with the catalytic functionality of Fe–N_x centers. The SiO_2-modified sample exhibits higher turnover frequencies (TOF), corroborating its enhanced intrinsic activity. Moreover, SiO_2/FeNSiC demonstrates competitive overall performance compared to other advanced ORR electrocatalysts, as summarized in Supplementary Table 5.

In situ characterization for stability enhancement analysis

To gain deeper insights into the ORR mechanism and the behavior of single-atom Fe active sites in FeNC catalysts with and without SiO_2 under ORR conditions, we conducted in situ XAS measurements (Supplementary Fig. 17a). Upon applying ORR-relevant potentials (from 0.9 to 0.3 V vs. RHE), we observed a significant reduction in the white-line peak intensity and a gradual shift of the adsorption edge to lower energy levels. This indicates a continuous reduction in the valence state of the single Fe center as the reaction progresses[57,58]. Notably, the near-edge spectrum obtained under open-circuit potential (OCP) closely resembled that of the initial catalyst state (Fig. 5a), suggesting that Fe–N_x sites remain coordinated to oxygen species under ambient conditions and OCP. This finding aligns with the expected thermodynamic stability of Fe–N_x configurations. The spectral evolution under applied potentials indicates that the reduction of Fe centers is primarily driven by cathodic polarization, facilitating the release of oxygen species from Fe–N_x sites[59,60]. A comparison of XANES edge behavior between the two samples (Fig. 5a, d) reveals that the SiO_2-free FeNSiC exhibits a larger edge shift of 1.35 eV and a lower potential onset than the SiO_2-modified counterpart. This indicates that redox transitions of Fe sites begin earlier (i.e., at higher overpotentials) in the absence of SiO_2. This behavior is attributed to the stabilizing effect of the SiO_2 matrix, which electronically and spatially passivates Fe–N_x sites, delaying their reduction. In particular, the presence of SiO_2 likely modulates the local electron density and alters oxygen adsorption/desorption kinetics, effectively shifting the redox onset toward lower overpotentials. Such observations are consistent with previous reports on support-induced electronic effects in Fe–N–C systems[46,61–63]. Further support is provided by DFT calculations presented later, which show that SiO_2 anchoring increases the demetalation energy barrier and modifies the electronic structure of Fe centers. While both samples were synthesized under identical conditions and show similar Fe loading and dispersion, the minor contributions from non-redox-active Fe species cannot be fully excluded. However, Mössbauer spectroscopy, XAS, XRD, and HAADF-STEM confirm that Fe is predominantly atomically dispersed in both samples. Thus, the observed edge-shift differences are more likely attributed to variations in the Fe–N_x environment and its interaction with the SiO_2 matrix, rather than to inactive Fe species.

The EXAFS spectrum at the Fe K-edge for the SiO_2-containing sample showed that the Fe–N bond length remained relatively stable, with the main peak centered at a reduced distance (R ≈ 1.41 Å, Fig. 5b). At a lower potential of 0.3 V, the Fe–N peak exhibited a slight negative shift (-0.07 Å), indicating a minor contraction of the Fe–N bond. To

https://doi.org/10.1038/s41467-025-65194-0

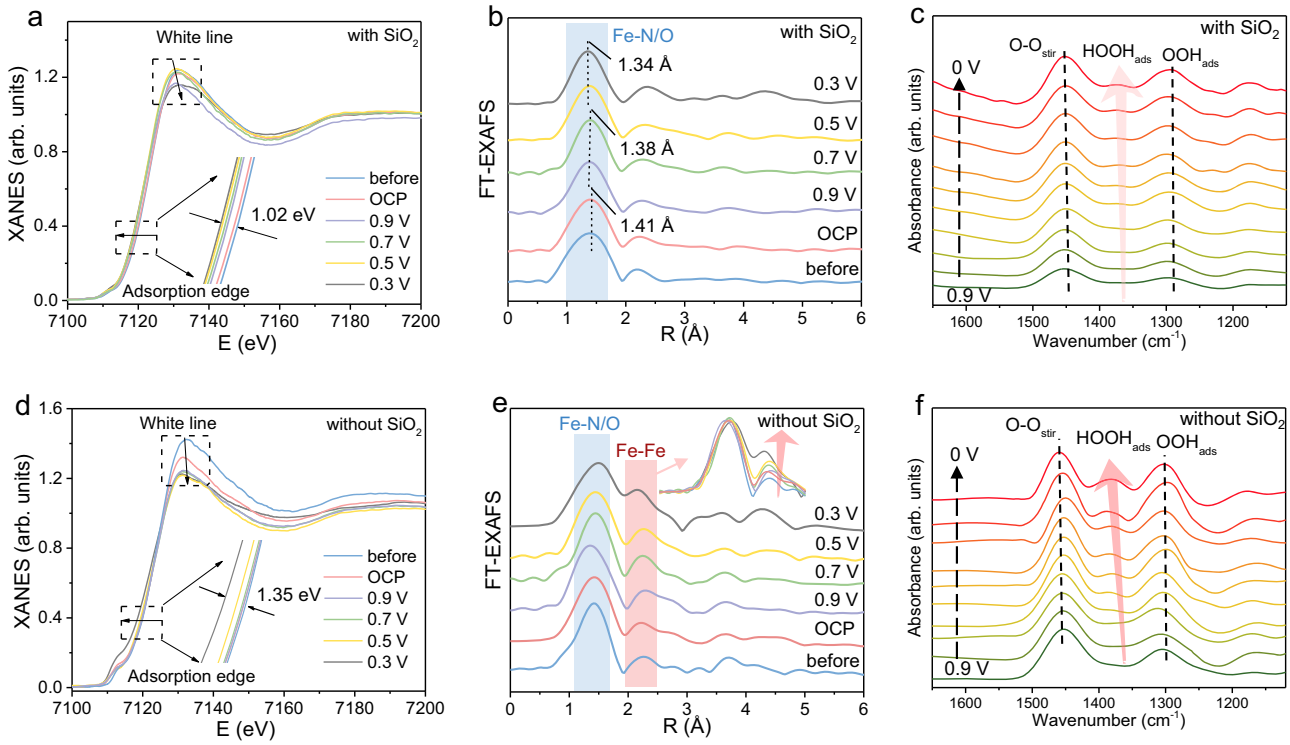

Fig. 5 | In situ XAFS and in situ ATR-IR measurements. a In situ X-ray absorption near-edge structure (XANES) of the Fe K-edge, (**b**) the corresponding Fourier transform k^3-weighted Fe K-edge extended X-ray absorption fine structure (FT-EXAFS) spectra and (**c**) In situ ATR-IR spectra were recorded on different potentials in 0.1 M KOH for FeNC SAC with and (**d**–**f**) without SiO_2 species (the change of bond length and intensity marked in the shadow area and arrow). Source data are provided as a Source Data file.

further elucidate the structural evolution of single-atom Fe active sites at various operating potentials, we conducted curve fitting analysis of the first shell for the Fe center of the sample with SiO_2. As revealed in Supplementary Fig. 15, the Fe–N_4 configuration can be nicely preserved despite voltage variations. In contrast, the FT-EXAFS spectra of the SiO_2-free sample (Fig. 5e, inset; Supplementary Fig. 16; Supplementary Table 6) exhibited an increasingly pronounced second-shell feature. The corresponding fitting results showed a clear increase in the coordination number of Fe–Fe bonds from 0.18 to 2.5 with decreasing potential, suggesting potential aggregation of Fe centers under reductive conditions, matching the Fe–Fe distance in Fe_2O_3 (marked by the arrow). These results suggest that Fe sites may undergo partial migration or dimerization in the absence of structural stabilization[46,62–64]. These findings highlight the crucial role of SiO_2 in preventing Fe aggregation and preserving the Fe–N_4 configuration during catalysis, thereby ensuring enhanced stability and performance.

Additionally, we conducted in situ attenuated total reflection-Fourier transform infrared (ATR-FTIR) measurements (see Supplementary Fig. 17b). Figure 5c reveals the emergence and intensification of major peaks at ~1453 cm^{-1} and ~1295 cm^{-1} (marked with dashed lines), along with a weak band at ~1373 cm^{-1} (red arrow), upon the application of negative-going potential steps on SiO_2/FeNSiC (Fig. 5c) and FeNSiC (Fig. 5f). These peaks can be attributed to the O–O stretching mode of adsorbed O_2 molecules, the surface-adsorbed OOH* (OOH_{ads}), and the OOH bending mode of the surface adsorbed *H_2O_2 ($HOOH_{ads}$), respectively[65,66]. Notably, compared to the SiO_2-free FeNSiC sample, the SiO_2/FeNSiC system exhibited a lower intensity of $HOOH_{ads}$ species, indicating a reduced tendency for H_2O_2 formation. Therefore, it can be inferred that SiO_2 plays a critical role in suppressing H_2O_2 production during ORR, the efficiency of the desired 4-electron pathway and enhancing overall ORR kinetics[67,68].

Theoretical insights into the stability improvement

To explore the role of SiO_2 in promoting the stability of the Fe–NC catalyst, DFT calculations were implemented. In our theoretical model, we constructed a $Si_{17}O_{34}$ cluster and obtained its representative amorphous configuration by the ab initio molecular dynamic (AIMD) simulation at 1173 K (see Supplementary Fig. 18 for details; AIMD trajectories shown in Supplementary Data 1). Supplementary Fig. 19 indicates that there are under-coordinated O atoms on the surface of the SiO_2 cluster, which tend to bind with the Fe center of the Fe–N_4 site. A favorable binding model was attained with a strong binding energy of −2.84 eV between the Fe–N_4 site and the representative configuration of amorphous $Si_{17}O_{34}$, which was employed in subsequent calculations (Supplementary Fig. 20). As depicted in Fig. 6a and Supplementary Figs. 21, 22, in the absence of a SiO_2 cluster, Fe atoms readily aggregate into Fe_2, a process that is not only exothermic but also nearly barrierless upon disruption of the N_4 coordination site. In contrast, when SiO_2 NPs are present, Fe aggregation becomes an endothermic process with a high energy barrier exceeding 2 eV. This indicates that SiO_2 effectively stabilizes the Fe–N_4 structure by preventing Fe single-atom aggregation, even when the Fe coordination site is perturbed. These results align well with the observations from the in situ XAS investigations.

The origin of the enhanced stability and activity of the SiO_2/FeNSiC catalyst in ORR was also investigated by DFT. The optimized 3D configurations of various ORR species (O*, O_2*, OH*, and OOH*) on the SAC with and without SiO_2 are depicted in Supplementary Fig. 23 (the atomic coordinates of optimized computational models are provided in Supplementary Data 1). The ORR free energy profiles in Fig. 6b and Supplementary Table 7 show that the free energy change of the H_2O_2 generation step (OOH* → H_2O_2) over the model with SiO_2 is 0.12 eV lower than that without SiO_2, indicating that the SiO_2 suppresses the generation of H_2O_2. Also, the strong binding between OOH* and Fe

https://doi.org/10.1038/s41467-025-65194-0

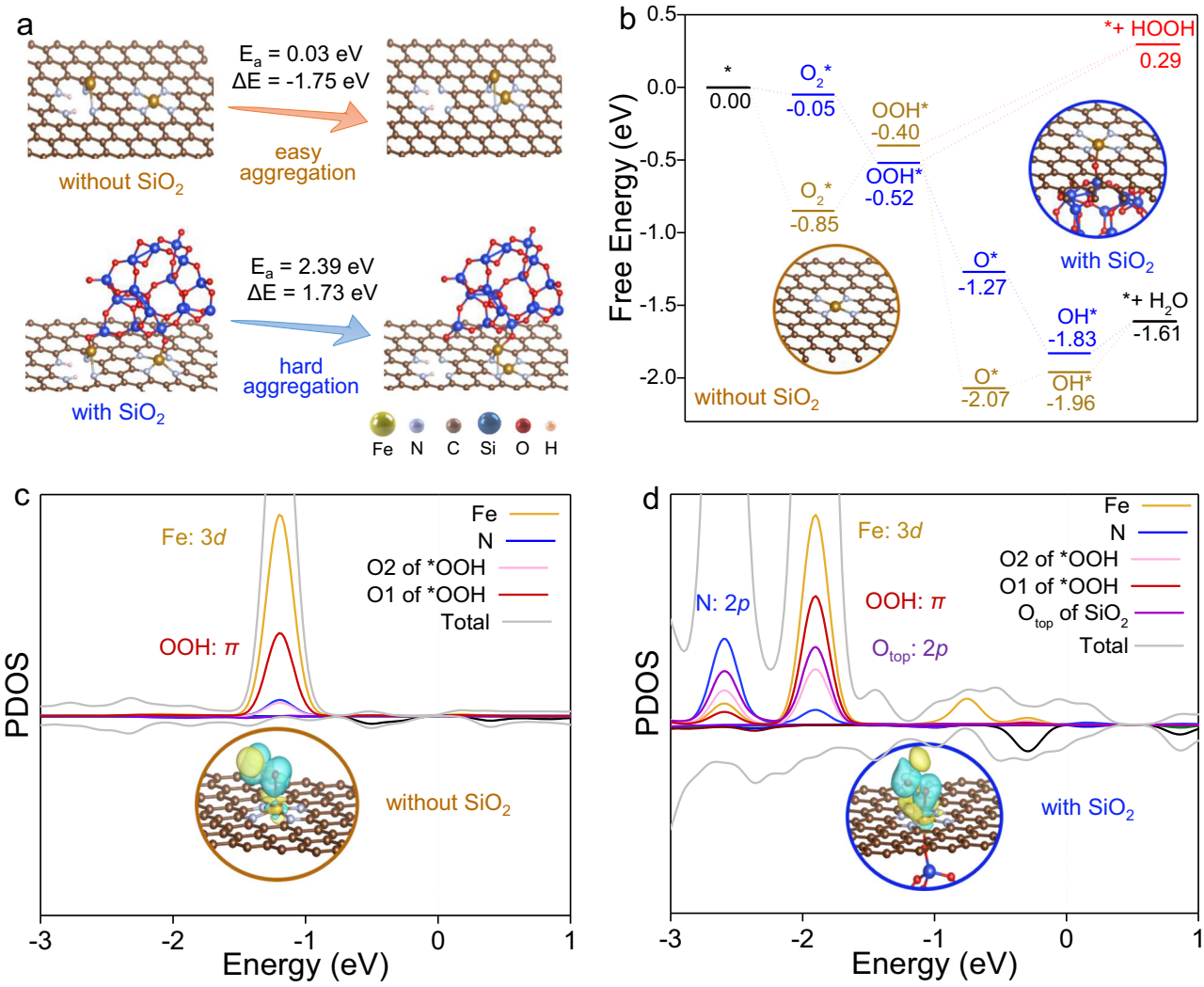

Fig. 6 | DFT calculations to elucidate the stability of samples with and without SiO_2. a DFT results of the energy change and energy barrier for the two Fe atoms aggregating into the Fe_2 NC with and without a SiO_2 cluster. Two H atoms were added on the damaged N_4 site to mimic the potential site break during the reaction. **b** The free energy profile for the ORR and the formation of H_2O_2. The projected density of state (PDOS) of OOH species over SAC (**c**) without and (**d**) with SiO_2 cluster. Source data are provided as a Source Data file.

center in the model with SiO_2 impedes its further conversion to the harmful ROS and H_2O_2, as suggested in previous studies[69–71]. Inhibiting the formation of attacking radicals and peroxide species could prevent the break of the Fe coordination site in the SAC[20–22]. Also, the vital step from OH* to H_2O is largely facilitated by the structure with SiO_2 (Fig. 6b), suggesting that the Fe-O-Si binding between SiO_2 NP and Fe center also favors the ORR activity.

To understand why the Fe-O-Si bond at the *trans* site of OOH induces the strong interaction between OOH* and the Fe–N_4 center, the interfacial electronic structure was dissected by projection density of states (PDOS) analysis. As indicated in Fig. 6c, without SiO_2 the π orbital of OOH overlaps with the Fe 3*d* orbital, to be more precise, mainly the Fe $3d_{yz}$ and $3d_{xz}$ orbitals (Supplementary Fig. 24). When the SiO_2 NP binds at the trans site of OOH, the O 2*p* orbital in the Fe–O–Si bond could have a superposition with the OOH π orbital, the Fe 3*d* orbital and even the N 2*p* orbital as displayed in Fig. 6d, that makes the stronger binding of OOH. There is also a stronger electron exchange between the OOH radical and Fe–N_4 site when SiO_2 NP is presented, by comparing the 3D isosurfaces in the circles of Fig. 6c, d. Thus, the SiO_2-Fe binding reinforces the interaction between OOH* species and the Fe–N_4 site, inhibiting the transformation of OOH* species into hazardous radicals or H_2O_2.

ZABs and PEMFCs performance and stability

The performance of SiO_2/FeNSiC as the oxygen cathode electrocatalyst was evaluated in a home-built zinc-air battery (ZAB) (Fig. 7a). The open-circuit voltage (OCV) results of the ZABs in Fig. 7b indicate that SiO_2/FeNSiC provides a higher value than Pt/C (1.47 V vs. 1.42 V). The practical potential of the two ZABs in tandem for electronic devices was demonstrated in Fig. 7b inset. They can power a light-emitting display (LED; 1.5 V) consecutively for a week. Figure 7c demonstrates that the rechargeable ZAB based on SiO_2/FeNSiC possesses polarization curves with a smaller voltage gap between charge and discharge, compared to that using Pt/C, indicating a higher energy efficiency and better rechargeable ability. Also, the ZAB assembled with SiO_2/FeNSiC exemplifies a power density of 195.9 mW cm^{-2}, surpassing that of Pt/C (100.3 mW cm^{-2}). The specific capacity of the ZAB, propelled by SiO_2/FeNSiC (Fig. 7d), stands at 765 mAh g^{-1} at 10 mA cm^{-2}, comparable to that based on Pt/C (749 mAh g^{-1}). The SiO_2/FeNSiC electrocatalyst was durable and reliable in a mechanically rechargeable battery, only requiring replacement of the electrolyte and consumed zinc anode after each discharge. Noticeably, no significant degradation occurred after 4 rounds throughout 160 h at a current density of 5 mA cm^{-2} (Fig. 7e). Furthermore, the SiO_2/FeNSiC-based battery (Fig. 7f and Supplementary Fig. 25) exhibited a

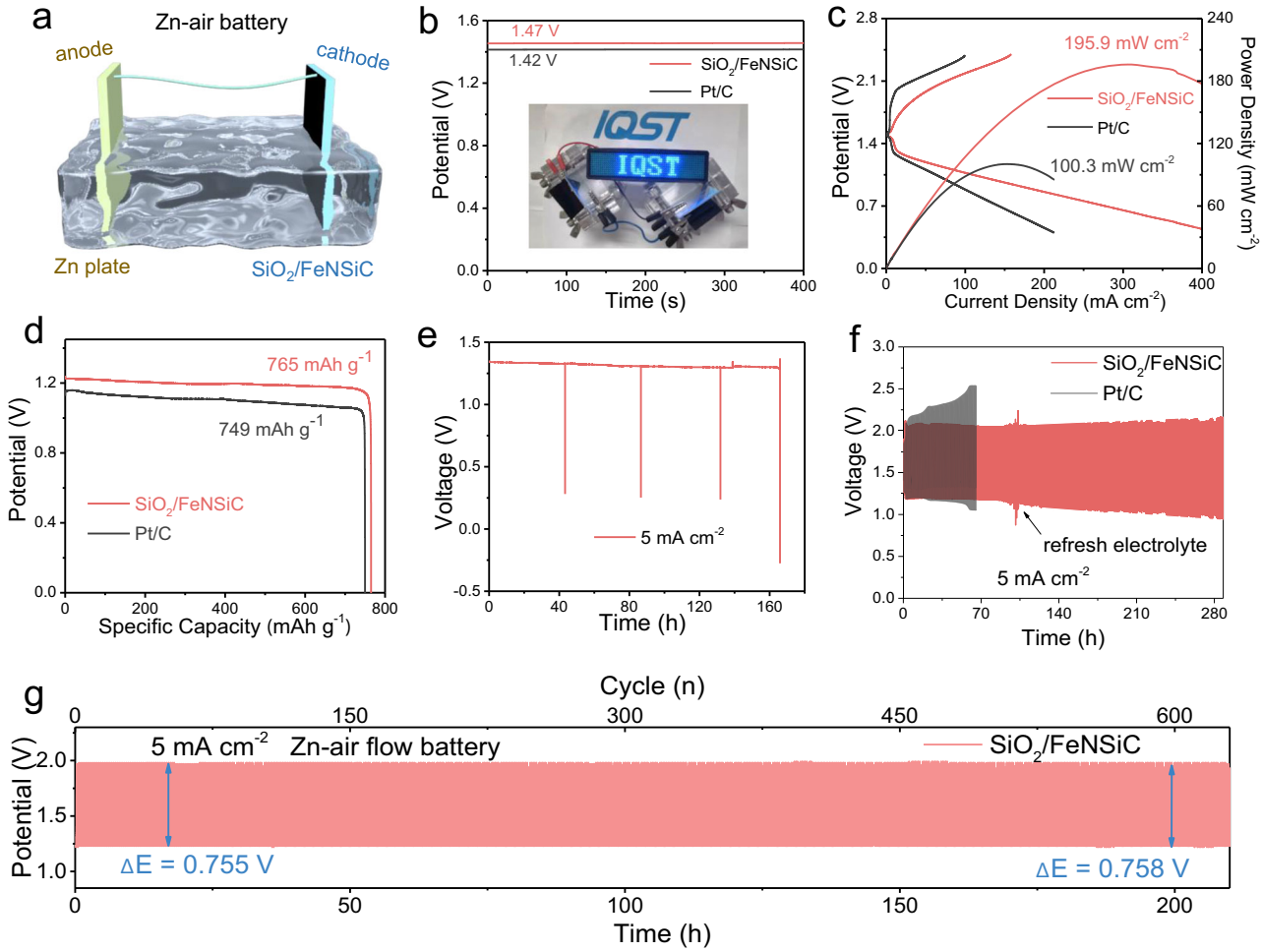

Fig. 7 | Performance of the SiO_2/FeNSiC catalyst in zinc-air batteries. **a** Schematic illustration of the homemade ZAB at 6 M KOH solution with 0.2 M $Zn(OAc)_2$. **b** OCV plots (inset: photo image of an LED light array powered by two ZABs in series). **c** Polarization charge and discharge plots and power density curves obtained from corresponding discharge polarization curves and (**d**) discharge plots at a current density of 10 mA cm^{-2} of the ZABs assembled with SiO_2/FeNSiC and Pt/C. **e** The constant current discharge curve of SiO_2/FeNSiC as an air cathode catalyst was used to evaluate the stability of SiO_2/FeNSiC. **f** Charging-discharging performance of the ZABs assembled with SiO_2/FeNSiC and Pt/C at 5 mA cm^{-2}. **g** Charging-discharging performance of the flow ZAB assembled with SiO_2/FeNSiC at 5 mA cm^{-2}. Source data are provided as a Source Data file.

consistently lower charge-discharge voltage gap and competitive long-term stability compared to batteries using Pt/C, FeNSiC, and FeNC without SiO_2. In light of potential electrolyte consumption, generated bubbles onto the cathode, and unstable interface arising from Zn anode passivation, we also evaluated the intrinsic activity of the SiO_2/FeNSiC catalyst using a flow ZAB (Fig. 7g and Supplementary Fig. 26). The SiO_2/FeNSiC-based flow battery delivered comparable durability than non-flow ZAB and other recent references (Supplementary Table 8). Notably, it maintained negligible round-trip efficiency loss even after 600 charge-discharge cycles over 200 h, underscoring the catalyst's operational longevity.

Beyond ZAB applications, we also evaluated the catalytic performance of FeNC-based catalysts in H_2-air proton exchange membrane fuel cells (PEMFCs). As depicted in Supplementary Fig. 27, the initial polarization and power density curves, along with their corresponding performance metrics following a 100-h durability test, are analyzed. Under 1.0 bar H_2-air conditions, the SiO_2/FeNSiC catalyst achieved a peak power density (P_{max}) of 379.6 mW cm^{-2}, surpassing FeNSiC (P_{max} = 370.5 mW cm^{-2}). Furthermore, during the 100-h stability test at a constant voltage of 0.5 V, the FeNSiC catalyst exhibited substantial performance degradation, whereas the SiO_2/FeNSiC catalyst maintained a much more stable electrochemical profile. This highlights the critical role of SiO_2 in enhancing both the stability and catalytic efficiency of the Fe–NC catalyst.

In summary, SiO_2 NP-decorated FeNC SACs have been synthesized using natural coffee grounds and industrial spent acid residues. The small SiO_2 NPs, derived from biomass, were uniformly distributed on the porous carbon substrate. The catalyst exhibits significantly improved stability and activity, thanks to the involvement of SiO_2 NPs in scavenging radicals and regulating the microstructure of the Fe centers. The binding of SiO_2 NP, and Fe sites prevents the aggregation of metal atoms and strengthens the interaction with OOH* species, eventually reducing the production yield of H_2O_2 during ORR, as validated by experiments and DFT calculations. This approach of using SiO_2 NPs as scavengers offers a promising strategy for designing more stable SACs for ORR and other systems involving H_2O_2 and oxidizing radicals.

Methods

Materials

Industrial spent acid (ISA) with a main composition of Fe^{3+} and HCl was obtained from Zhejiang Viersin New Material Co. Ltd., Jiaxing, China. Zinc acetate ($Zn(Ac)_2$, AR, 98%), ethanol, potassium hydroxide (KOH, AR, 99.99%), potassium chloride (KCl, AR, 99%), HF (AR, >40%), and HCl (AR, ~37%) were obtained from Sinopharm Chemical Reagent Co.,

Ltd. No additional purification was performed before using any of the chemicals. A Millipore water system with 18.2 MΩ·cm resistivity at 25 °C was used to produce deionized (DI) water. Coffee grounds (CGs) were collected from the waste of commercial products of GROUND ROASTED COFFEE, FULL BODIED, illy blend™ (100% ARABICA), illycaffè S.p.A, Italy.

Catalyst synthesis

The CGs were first purified by repeated rinsing with DI water and then vacuum-dried at 80 °C for 72 h to remove residual moisture[41]. The resulting powder was treated in spent acid for 24 h, freeze-dried, and subsequently carbonized with urea (mass ratio; 1:1) in a N_2-purged tubular furnace at 900 °C for 2 h, with a heating rate of 5 °C min^{-1}. The pyrolyzed product was further leached in HCl for 12 h to dissolve unstable Fe clusters, thoroughly rinsed with DI water, and collected as the SiO_2/FeNSiC composite. Residual silica domains were eliminated by HF etching to obtain FeNSiC. A reference FeNC catalyst was prepared by following the same procedure, except that HF-pretreated CGs were used as the precursor to eliminate Si species prior to pyrolysis.

Electrochemical evaluation

Electrochemical measurements were conducted using a standard three-electrode configuration, with data acquisition performed by a CHI760e electrochemical workstation (CH Instruments, USA). A rotating ring-disk electrode (RRDE; Pine Instrument) with a 5 mm glassy carbon disk and a gold ring (6.5 mm inner, 7.5 mm outer diameter) served as the working electrode. The counter electrode is a graphite rod, while the reference electrode is Ag/AgCl, in which the internal electrolyte is a saturated KCl solution. All glassware and electrodes were rigorously pre-treated (including aqua regia cleaning and ultrapure water rinsing).

The catalyst ink was prepared by ultrasonically dispersing a mixture containing 5 mg of catalyst, 0.3 mL of H_2O, 0.7 mL of ethanol, and 40 µL of 5% Nafion solution for 30 min to achieve homogeneity. The resulting ink was drop-cast onto the electrode surface and dried to form a uniform catalyst layer. Electrochemical measurements were performed using cyclic voltammetry (CV) under N_2 or O_2 atmosphere (scan rate: 50 mV s^{-1}) and linear sweep voltammetry (LSV) in O_2-saturated freshly-prepared 0.1 M KOH electrolyte prepared with ultrapure water and stored in a sealed container at room temperature (pH = 13.0 ± 0.2; the resistance of the solution was 50 ± 3 Ω; scan rate: 10 mV s^{-1}; rotational speed: 1600 rpm). Acidic ORR measurements were performed in O_2-saturated 0.5 M H_2SO_4 (pH = 0.3 ± 0.2) with a solution resistance of 15 ± 2 Ω.

The electron transfer number (n) and the yield of the intermediate (HO_2^-) during the ORR process were obtained from rotating ring-disk electrode measurements and calculated by the following equations:

$$n = \frac{4I_d}{I_d + \left(\frac{I_r}{N}\right)} \tag{1}$$

$$\%H_2O_2 = \frac{200\left(\frac{I_r}{N}\right)}{I_d + \left(\frac{I_r}{N}\right)} \tag{2}$$

where I_d, I_r, and N denote disk current, ring current and collection efficiency of Pt ring (0.37), respectively. All the recorded potentials were corrected to RHE using the following equation without iR-compensation:

$$E_{RHE} = E_{Ag/AgCl} + 0.059 \times pH + 0.197 \tag{3}$$

where E_{RHE} and $E_{Ag/AgCl}$ refer to the potential relevant to a reversible hydrogen electrode (RHE) and Ag/AgCl electrode, respectively.

The Fe–N_x site density in FeNC-SACs was quantitatively determined through nitrite (NO_2^-) adsorption and reduction analysis following Kucernak's methodology[72]. The experiments were conducted in three stages: (1) ORR LSV curves and nitrite reduction CV were measured without NO_2^- to obtain background data; (2) the same measurements were performed with NO_2^- present; (3) additional experiments without NO_2^- were carried out to study catalyst recovery for ORR. The site density (SD) and turnover frequency (TOF) were calculated using the following equations[72,73]:

$$SD\left(site\,g^{-1}\right) = \frac{Q_{strip} \times N_A}{n_{strip} \times F \times m_{cat}} \tag{4}$$

$$TOF\left(s^{-1}\right) = \frac{n_{strip} \times \Delta j_k\left(mA\,cm^{-2}\right)}{Q_{strip}\left(Cg^{-1}\right) \times L_c\left(mg\,cm^{-2}\right)} \tag{5}$$

$$j_k = \frac{j_{lim} \times j}{j_{lim} - j} \tag{6}$$

$$\Delta j_k = j_{k(unpoisoned)} - j_{k(poisoned)} \tag{7}$$

where Q_{strip} (C g^{-1}) is the excess coulometric charge from the stripping voltammogram, N_A denotes Avogadro constant ($N_A = 6.02 \times 10^{23}$), F stands for the Faraday constant (F = 96485 C mol^{-1}), n_{strip} indicates the electron transfer number involved in NO_2^- reduction per active site (n_{strip} = 5), m_{cat} (g) is the mass of the catalyst, L_c is the catalyst loading during the reversible nitrite poisoning experiments (0.27 mg cm^{-2}). To quantify the active site density, all measurements were performed in a 0.5 M acetate buffer at pH = 5.2.

Characterization

A JEOL-7800F SEM and Talos F200X TEM were used to image the morphology of the samples. HAADF-STEM was conducted at Shanghai, ThermoFisher Scientific. N_2 adsorption/desorption analysis was measured at 77 K on an AUTOSORB IQ Instrument, Quantachrome. XRD patterns were characterized using a Bruker D8 with the X-ray source being Cu-Kα radiation operated at 3 kV. ICP-OES was tested with Agilent 720ES. The stationary XAFS test was carried out at the BL08B2* of SPring-8 (8 GeV, 100 mA) in Japan, where the X-ray beam was monochromatized with a water-cooled Si (111) double-crystal monochromator and focused with two Rh-coated focusing mirrors with the beam size of 2.0 mm in the horizontal direction and 0.5 mm in the vertical direction around the sample position. XPS measurements were performed on ESCALAB Xi+. Raman spectra were collected with a Thermo Fisher DXR with a wavelength of 532 nm. PL spectra were conducted on an FS5 Spectrophotometer. The EPR test was determined using a Bruker A-300 spectrometer using DMPO as the trapping agent. In situ electrochemical ATR-FTIR was conducted on a Shanghai Linglu Instruments ElectroChem IR cell equipped with a Pike VeeMAX™ III ATR. Data were collected with a Nicolet iS50 FT-IR spectrometer using a mercury-cadmium-telluride (MCT) detector cooled by liquid N_2, and Au-modified single bounce silicon served as a cathode. In situ XAFS spectroscopy was carried out using the Rapid-XAFS 2 M (Anhui Absorption Spectroscopy Analysis Instrument Co., Ltd.) by transmission (or fluorescence) mode at 20 kV and 20 mA, and the Ge (620) spherically bent crystal analyzer with a radius of curvature of 500 mm was used for Fe. Room-temperature ^{57}Fe Mössbauer spectra were recorded using a ^{57}Co/Rh source and a triangular velocity waveform spectrometer equipped with a NaI detector, with velocity calibration performed using an α-Fe foil. The optical absorption properties were characterized by UV–vis spectroscopy using a Shimadzu UV-3600i Plus spectrophotometer.

X-ray absorption spectra were processed using the ATHENA software package. For XANES analysis, the pre-edge background was removed, and spectra were normalized by extrapolating a quadratic polynomial fitted to the post-edge region, following the AUTOBK algorithm[74]. EXAFS signals, $\chi(k)$, were extracted from the normalized spectra using standard procedures. To enhance contributions from higher-k components, the data were weighted by k^3 before Fourier transformation, which was carried out using a Hanning window function to minimize truncation effects. Quantitative EXAFS analysis was performed using ARTEMIS[75], with theoretical scattering paths generated by the FEFF9 code[76]. The Fe–N ([FeN_mp-6988_computed] N1.1) path was calculated using FeN crystal, the Fe–O ([Fe_2SiO_4] O24.1_) and Fe–Si ([Fe_2SiO_4] Si9.1_) paths were calculated using the fayalite (Fe_2SiO_4) crystal structure model, as it serves as a representative structural model for the Fe–O–Si coordination motif. These models provided reliable theoretical references for simulating the local atomic environments around Fe atoms. The fitting was performed over a k-range of 2.5–12 $Å^{-1}$. The amplitude reduction factor (S_0^2) was fixed at 0.79 for Fe, determined from fitting metallic Fe reference foils, and coordination numbers were constrained based on the respective crystal structures used for each path.

EPR and FL spectroscopy for radical scavenging evaluation

Hydroxyl radicals (•OH) were generated through the Fenton reaction using 9 M of H_2O_2 and $FeSO_4$ as reactants, with 100 mM DMPO serving as the spin-trapping agent for radical identification. The reaction system was prepared by sequential addition of deionized water, H_2O_2, DMPO, and $FeSO_4$, followed by pH adjustment to ~3 using H_2SO_4. Comparative experiments were conducted without and with the SiO_2 scavengers. EPR measurements were immediately performed after reaction initiation using capillary-loaded samples. Parallel radical detection was achieved through a non-fluorescent coumarin-based molecular probe that undergoes conversion to highly fluorescent 7-hydroxycoumarin upon •OH oxidation. In a typical experiment, the 5 mL of coumarin solution (0.5 mM, dissolved in 0.1 M H_2SO_4) was introduced to acidic electrolytes after the chronoamperometric method (i–t) test, the temporal fluorescence evolution of coumarin derivatives was then quantified by monitoring intensity variations relative to baseline values using a fluorescence spectrophotometer. The radical scavenging activity of FeNC-based catalysts was assessed using ABTS as a probe. Catalysts (4 mg) were dispersed in 5 mL of 0.1 M H_2SO_4 by ultrasonication. ABTS• + radicals were initiated by combining 5 mL of 2 mM ABTS with 5 mL of 10 mM H_2O_2 in 0.1 M H_2SO_4 for 10 min, followed by 50-fold dilution. The catalyst suspension was then added to 2 mL of the diluted ABTS• + solution and reacted for 5 min. Radical scavenging efficiency was quantified through absorbance measurement at 417 nm using UV-vis spectroscopy.

Zinc-air battery measurements

The ZAB was constructed using 0.3 mm of polished zinc foil (1 × 3 cm) as the anode. The air cathode was fabricated by coating carbon paper with a catalyst ink containing 10 mg catalyst, 200 µL of 5% Nafion solution, 1.5 mL of ethanol, and 0.5 mL of H_2O, followed by 30 min ultrasonic dispersion and hot-pressing at 80 °C to achieve a catalyst loading of 2 mg cm^{-2}. For reference, commercial 20 wt% Pt/C catalysts were deposited onto carbon paper at a mass loading of 1.0 mg cm^{-2} and employed as the air electrode in the ZABs. The electrode assembly was vacuum-dried at 60 °C for 2 h before testing. A mixed electrolyte of 6 M KOH and 0.2 M $ZnCl_2$ was employed. Polarization curves were acquired via LSV at 10 mV s^{-1}, while cycling stability was evaluated through galvanostatic charge-discharge tests at 5 mA cm^{-2} (10 min charge/10 min discharge per cycle) using an electrochemical workstation (CS 2350 bipotentiostat; Wuhan Corrtest Instrument Co., Ltd).

The power density was determined using the following equation:

$$\text{power density} = \text{current density} \times \text{voltage} \tag{8}$$

The specific capacity was derived from the following equation:

$$\text{specific capacity} = \frac{\text{current} \times \text{test hours}}{\text{consumed zinc plate mass}} \tag{9}$$

PEMFC tests

The Fe–N–C catalyst ink was formulated by dispersing 5 wt% of Nafion (Sigma-Aldrich) in isopropanol/deionized water (2:1, v/v) followed by sequential 2 h ultra-sonication and magnetic stirring to achieve homogeneity, then brush-coated onto carbon paper (5 cm^2, GDS2240, Ballard) with a loading of 3 mg cm^{-2} as the cathode and vacuum-dried at 80 °C for 2 h before blade-coating onto a Nafion NR211 membrane, while the anode was fabricated with commercial 40 wt% Pt/C (0.2 mg_{Pt} cm^{-2}). Fuel cell tests were conducted on an 850e station (Scribner) under controlled conditions: 2-h membrane hydration with humidified N_2 (100% relative humidity, 0.5 L min^{-1}) at 80 °C, followed by H_2/air operation (300/500 mL min^{-1}, 1 bar) at 80 °C with 100 h durability assessment at 0.5 V constant voltage.

Computational details

The DFT calculations were carried out with the Vienna ab initio simulation package (VASP) under periodic boundary conditions[77]. The interactions between ions and core electrons were treated using the projector-augmented wave (PAW) approach, and the exchange–correlation energy was described by the generalized gradient approximation with the Perdew–Burke–Ernzerhof (PBE) functional[78,79]. Long-range dispersion interactions were accounted for using the DFT-D3 correction proposed by Grimme[80]. The simulation cell dimensions were 17.22 Å × 17.04 Å × 20.00 Å, for which Γ-point sampling of the Brillouin zone was adopted. A plane-wave cutoff of 400 eV was applied. Electronic self-consistent iterations[81] were converged to 1×10^{-7} eV, and atomic relaxations were performed until the maximum force on each atom was below 0.05 eV $Å^{-1}$. Transition-state (TS) searches and migration barrier calculations were performed using the climbing-image nudged elastic band (CI-NEB) method[82].

For the ORR process, based on the following steps, the four-electrons pathway as follows[83,84]:

$$O_2(g) + * \rightarrow O_2^* \tag{10}$$

$$O_2^* + H_2O(l) + e^- \rightarrow OOH^* + OH \tag{11}$$

$$OOH^* + e^- \rightarrow O^* + OH \tag{12}$$

$$O^* + H_2O(l) + e^- \rightarrow OH^* + OH \tag{13}$$

$$OH^* + e^- \rightarrow OH^* + * \tag{14}$$

The equation of (10–14) represent the four successive electron-transfer steps involved in the ORR. The reaction free energy change (ΔG) for each elementary step was evaluated using

$$\Delta G = \Delta H - T\Delta S - qU + kBT\ln 10 \times pH \tag{15}$$

where ΔH is the enthalpy change obtained from the reaction energy (ΔE) corrected by zero-point energy (ZPE) within DFT calculations; The term $T\Delta S$ accounts for entropy contributions; U is the applied

electrode potential, and q denotes the number of electrons transferred per step ($-|e|$).

Data availability

The data that support the findings of this study are available within the article and its Supplementary Information files. All other data supporting the findings of this study are available from the corresponding authors upon request. Source data are provided with this paper.

References

1. Zaman, S. et al. Oxygen reduction electrocatalysts toward practical fuel cells: progress and perspectives. *Angew. Chem. Int. Ed.* **60**, 17832–17852 (2021).
2. Tian, X., Lu, X. F., Xia, B. Y. & Lou, X. W. Advanced electrocatalysts for the oxygen reduction reaction in energy conversion technologies. *Joule* **4**, 45–68 (2020).
3. Wu, M. et al. Aqueous Zn-based rechargeable batteries: recent progress and future perspectives. *InfoMat*. **4**, e12265 (2022).
4. Dong, F. et al. Atomically dispersed transition metal-nitrogen-carbon bifunctional oxygen electrocatalysts for zinc-air batteries: recent advances and future perspectives. *Nano-Micro Lett* **14**, 36 (2021).
5. Strickland, K. et al. Highly active oxygen reduction non-platinum group metal electrocatalyst without direct metal–nitrogen coordination. *Nat. Commun.* **6**, 7343 (2015).
6. Li, Y. et al. An oxygen reduction electrocatalyst based on carbon nanotube–graphene complexes. *Nat. Nanotechnol.* **7**, 394–400 (2012).
7. Zago, S., Scarpetta-Pizo, L. C., Zagal, J. H. & Specchia, S. PGM-free biomass-derived electrocatalysts for oxygen reduction in energy conversion devices: promising materials. *Electrochem. Energy Rev.* **7**, 1 (2024).
8. Wang, Q. et al. Tailoring the microenvironment in Fe–N–C electrocatalysts for optimal oxygen reduction reaction performance. *Sci. Bull.* **67**, 1264–1273 (2022).
9. Wu, M. et al. Electronic metal–support interaction modulation of single-atom electrocatalysts for rechargeable zinc–air batteries. *Small Methods* **6**, 2100947 (2022).
10. Liu, M. et al. Fe-NC Single-atom catalyst with hierarchical porous structure and P–O bond coordination for oxygen reduction. *ACS Energy Lett.* **8**, 4531–4539 (2023).
11. Shao, W. et al. Carbon-based electrodes for advanced zinc-air batteries: oxygen-catalytic site regulation and nanostructure design. *Electrochem. Energy Rev.* **6**, 11 (2023).
12. Lefèvre, M., Proietti, E., Jaouen, F. & Dodelet, J.-P. Iron-based catalysts with improved oxygen reduction activity in polymer electrolyte fuel cells. *Science* **324**, 71–74 (2009).
13. Zhang, G. et al. Non-PGM electrocatalysts for PEM fuel cells: effect of fluorination on the activity and stability of a highly active NC_Ar + NH_3 catalyst. *Energy Environ. Sci.* **12**, 3015–3037 (2019).
14. Bae, G. et al. Unravelling the complex causality behind Fe–N–C degradation in fuel cells. *Nat. Catal.* **6**, 1140 (2023).
15. Shao, Y., Dodelet, J.-P., Wu, G. & Zelenay, P. PGM-free cathode catalysts for PEM fuel cells: a mini-review on stability challenges. *Adv. Mater.* **31**, 1807615 (2019).
16. Choi, C. H. et al. The Achilles' heel of iron-based catalysts during oxygen reduction in an acidic medium. *Energy Environ. Sci.* **11**, 3176–3182 (2018).
17. Liu, S. et al. Operando deconvolution of the degradation mechanisms of iron–nitrogen–carbon catalysts in proton exchange membrane fuel cells. *Energy Environ. Sci.* **16**, 3792–3802 (2023).
18. Ma, Q. et al. Stabilizing Fe–N–C catalysts as model for oxygen reduction reaction. *Adv. Sci.* **8**, 2102209 (2021).
19. Wu, M. et al. Emerging atomically precise metal nanoclusters and ultrasmall nanoparticles for efficient electrochemical energy catalysis: synthesis strategies and surface/interface engineering. *Electrochem. Energy Rev.* **7**, 10 (2024).
20. Zhang, G., Chenitz, R., Lefèvre, M., Sun, S. & Dodelet, J.-P. Is iron involved in the lack of stability of Fe/N/C electrocatalysts used to reduce oxygen at the cathode of PEM fuel cells? *Nano Energy* **29**, 111–125 (2016).
21. Jaouen, F. O_2 Reduction mechanism on non-noble metal catalysts for PEM fuel cells. Part II: a porous-electrode model to predict the quantity of H_2O_2 detected by rotating ring-disk electrode. *J. Phys. Chem. C.* **113**, 15433–15443 (2009).
22. Goellner, V., Armel, V., Zitolo, A., Fonda, E. & Jaouen, F. Degradation by hydrogen peroxide of metal-nitrogen-carbon catalysts for oxygen reduction. *J. Electrochem. Soc.* **162**, H403 (2015).
23. Yu, J., Su, C., Shang, L. & Zhang, T. Single-atom-based oxygen reduction reaction catalysts for proton exchange membrane fuel cells: progress and perspective. *ACS Nano*. **17**, 19514–19525 (2023).
24. Ramaswamy, N., Tylus, U., Jia, Q. & Mukerjee, S. Activity descriptor identification for oxygen reduction on nonprecious electrocatalysts: linking surface science to coordination chemistry. *J. Am. Chem. Soc.* **135**, 15443–15449 (2013).
25. Xia, D. et al. Degradation and regeneration of Fe–N_x active sites for the oxygen reduction reaction: the role of surface oxidation, Fe demetallation and local carbon microporosity. *Chem. Sci.* **12**, 11576–11584 (2021).
26. Qu, X. et al. Stepwise pyrolysis treatment as an efficient strategy to enhance the stability performance of Fe-N_x/C electrocatalyst towards oxygen reduction reaction and proton exchange membrane fuel cell. *Appl. Catal. B.* **295**, 120311 (2021).
27. Wan, X. et al. Iron atom–cluster interactions increase activity and improve durability in Fe–N–C fuel cells. *Nat. Commun.* **13**, 2963 (2022).
28. Xie, H. et al. Ta–TiO_x nanoparticles as radical scavengers to improve the durability of Fe–N–C oxygen reduction catalysts. *Nat. Energy* **7**, 281–289 (2022).
29. Cheng, X. et al. Instantaneous free radical scavenging by CeO_2 nanoparticles adjacent to the Fe–N_4 active sites for durable fuel cells. *Angew. Chem. Int. Ed.* **62**, e202306166 (2023).
30. Ji, M., He, B., Yu, Y., Yu, X. & Xing, S. CeO_2 encapsulated by iron, sulfur, and nitrogen-doped carbons for enhanced oxygen reduction reaction catalytic activity. *ChemElectroChem* **7**, 642–648 (2020).
31. Li, J.-C. et al. Stabilizing single-atom iron electrocatalysts for oxygen reduction via ceria confining and trapping. *ACS Catal.* **10**, 2452–2458 (2020).
32. Prabhakaran, V., Arges, C. G. & Ramani, V. Investigation of polymer electrolyte membrane chemical degradation and degradation mitigation using in situ fluorescence spectroscopy. *Prog. Nat. Sci.: Mater. Int.* **109**, 1029–1034 (2012).
33. Qiu, Y. et al. Improvement in ORR durability of Fe single-atom carbon catalysts hybridized with CeO_2 nanozyme. *Nano Lett* **24**, 9034–9041 (2024).
34. Rui, Z. & Liu, J. Understanding of free radical scavengers used in highly durable proton exchange membranes. *Prog. Nat. Sci.: Mater. Int.* **30**, 732–742 (2020).
35. Liu, M. et al. In-situ silica xerogel assisted facile synthesis of Fe-N-C catalysts with dense Fe-N_x active sites for efficient oxygen reduction. *Small* **18**, 2104934 (2022).
36. Jiao, L. et al. Nanocasting SiO_2 into metal–organic frameworks imparts dual protection to high-loading Fe single-atom electrocatalysts. *Nat. Commun.* **11**, 2831 (2020).
37. Chen, G. et al. Zinc-mediated template synthesis of Fe-N-C electrocatalysts with densely accessible Fe-N_x active sites for efficient oxygen reduction. *Adv. Mater.* **32**, 1907399 (2020).
38. Epstein, E. Silicon: its manifold roles in plants. *Ann. Appl. Biol.* **155**, 155–160 (2009).

39. Parecido, R. J., Soratto, R. P., Perdoná, M. J. & Gitari, H. I. Foliar-applied silicon may enhance fruit ripening and increase yield and nitrogen use efficiency of Arabica coffee. *Eur. J. Agron.* **140**, 126602 (2022).
40. Savvas, D. & Ntatsi, G. Biostimulant activity of silicon in horticulture. *Sci. Hortic.* **196**, 66–81 (2015).
41. Liu, M. et al. Nanoporous-structured Fe-NC single-atom electrocatalysts based on lotus seedpods and industrial acid residues for efficient oxygen reduction reaction. *ACS Appl. Nano Mater.* **6**, 14831–14840 (2023).
42. Xiao, M. et al. Engineering energy level of metal center: ru single-atom site for efficient and durable oxygen reduction catalysis. *J. Am. Chem. Soc.* **141**, 19800–19806 (2019).
43. Lin, L., Zhu, Q. & Xu, A.-W. Noble-metal-free Fe–N/C catalyst for highly efficient oxygen reduction reaction under both alkaline and acidic conditions. *J. Am. Chem. Soc.* **136**, 11027–11033 (2014).
44. Zhang, H. et al. Single atomic iron catalysts for oxygen reduction in acidic media: particle size control and thermal activation. *J. Am. Chem. Soc.* **139**, 14143–14149 (2017).
45. Wei, Q. et al. An active and robust Si-Fe/N/C catalyst derived from waste reed for oxygen reduction. *Appl. Catal. B.* **237**, 85–93 (2018).
46. Zitolo, A. et al. Identification of catalytic sites for oxygen reduction in iron- and nitrogen-doped graphene materials. *Nat. Mater.* **14**, 937–942 (2015).
47. Song, R. et al. O, N-Codoped 3D graphene hollow sphere derived from metal–organic frameworks as oxygen reduction reaction electrocatalysts for Zn-air batteries. *Nanoscale* **13**, 6174–6183 (2021).
48. Jia, Q. et al. Experimental observation of redox-induced Fe–N switching behavior as a determinant role for oxygen reduction activity. *ACS Nano* **9**, 12496–12505 (2015).
49. Marshall-Roth, T. et al. A pyridinic Fe-N_4 macrocycle models the active sites in Fe/N-doped carbon electrocatalysts. *Nat. Commun.* **11**, 5283 (2020).
50. Wang, J. et al. Design of N-coordinated dual-metal sites: a stable and active Pt-free catalyst for acidic oxygen reduction reaction. *J. Am. Chem. Soc.* **139**, 17281–17284 (2017).
51. Wang, J. et al. Synergistic effect of well-defined dual sites boosting the oxygen reduction reaction. *Energy Environ. Sci.* **11**, 3375–3379 (2018).
52. Zhao, X. et al. Selenite capture by MIL-101 (Fe) through FeOSe bonds at free coordination Fe sites. *J. Hazard. Mater.* **424**, 127715 (2022).
53. Peng, L. et al. Mesopore-rich Fe–N–C catalyst with FeN_4–O–NC single-atom sites delivers remarkable oxygen reduction reaction performance in alkaline media. *Adv. Mater.* **34**, 2202544 (2022).
54. Chen, Z. et al. Fe_1N_4–O_1 site with axial Fe–O coordination for highly selective CO_2 reduction over a wide potential range. *Energy Environ. Sci.* **14**, 3430–3437 (2021).
55. Zhong, L. et al. Wood carbon based single-atom catalyst for rechargeable Zn–Air batteries. *ACS Energy Lett* **6**, 3624–3633 (2021).
56. Liu, Z. et al. Highly stable and active flexible electrocatalysts derived from lotus fibers. *Adv. Funct. Mater.* **33**, 2211563 (2023).
57. Wu, B. et al. In situ x-ray absorption spectroscopy of metal/nitrogen-doped carbons in oxygen electrocatalysis. *Angew. Chem. Int. Ed.* **62**, e202219188 (2023).
58. Tylus, U. et al. Elucidating oxygen reduction active sites in pyrolyzed metal–nitrogen coordinated non-precious-metal electrocatalyst systems. *J. Phys. Chem. C* **118**, 8999–9008 (2014).
59. Zhou, W. et al. Identification of the evolving dynamics of coordination-unsaturated iron atomic active sites under reaction conditions. *ACS Energy Lett* **6**, 3359–3366 (2021).
60. Cui, K. et al. Crystalline dual-porous covalent triazine frameworks as a new platform for efficient electrocatalysis. *Angew. Chem. Int. Ed.* **63**, e202317664 (2024).
61. Zitolo, A. et al. Identification of catalytic sites in cobalt-nitrogen-carbon materials for the oxygen reduction reaction. *Nat. Commun.* **8**, 957 (2017).
62. Mehmood, A. et al. High loading of single atomic iron sites in Fe–NC oxygen reduction catalysts for proton exchange membrane fuel cells. *Nat. Catal.* **5**, 311–323 (2022).
63. Li, J. et al. Identification of durable and non-durable FeN_x sites in Fe–N–C materials for proton exchange membrane fuel cells. *Nat. Catal.* **4**, 10–19 (2021).
64. Zhang, N. et al. High-density planar-like Fe_2N_6 structure catalyzes efficient oxygen reduction. *Matter* **3**, 509–521 (2020).
65. Nayak, S., McPherson, I. J. & Vincent, K. A. Adsorbed intermediates in oxygen reduction on platinum nanoparticles observed by in situ IR spectroscopy. *Angew. Chem. Int. Ed.* **57**, 12855–12858 (2018).
66. Mondal, S. et al. In situ mechanistic insights for the oxygen reduction reaction in chemically modulated ordered intermetallic catalyst promoting complete electron transfer. *J. Am. Chem. Soc.* **144**, 11859–11869 (2022).
67. Hu, J. et al. Uncovering dynamic edge-sites in atomic Co–N–C electrocatalyst for selective hydrogen peroxide production. *Angew. Chem. Int. Ed.* **62**, e202304754 (2023).
68. Li, Y. et al. Single-atom iron catalyst with biomimetic active center to accelerate proton spillover for medical-level electrosynthesis of H_2O_2 disinfectant. *Angew. Chem. Int. Ed.* **62**, e202306491 (2023).
69. Chu, Y. et al. Dual single-atom catalyst design to build robust oxygen reduction electrode via free radical scavenging. *Chem Catal.* **3** (2023).
70. Xia, P. et al. Tailoring single-atom FeN4 moieties as a robust heterogeneous catalyst for high-performance electro-Fenton treatment of organic pollutants. *Appl. Catal. B* **322**, 122116 (2023).
71. Zhao, J. et al. Manipulating the oxygen reduction reaction pathway on Pt-coordinated motifs. *Nat. Commun.* **13**, 685 (2022).
72. Malko, D., Kucernak, A. & Lopes, T. In situ electrochemical quantification of active sites in Fe–N/C non-precious metal catalysts. *Nat. Commun.* **7**, 13285 (2016).
73. Wan, X. et al. Fe–N–C electrocatalyst with dense active sites and efficient mass transport for high-performance proton exchange membrane fuel cells. *Nat. Catal.* **2**, 259–268 (2019).
74. Newville, M. IFEFFIT: interactive XAFS analysis and FEFF fitting. *J. Synchrotron Radiat.* **8**, 322–324 (2001).
75. Ravel, B. & Newville, M. ATHENA, ARTEMIS, HEPHAESTUS: data analysis for X-ray absorption spectroscopy using IFEFFIT. *J. Synchrotron Radiat.* **12**, 537–541 (2005).
76. Rehr, J. J., Kas, J. J., Vila, F. D., Prange, M. P. & Jorissen, K. Parameter-free calculations of X-ray spectra with FEFF9. *Phys. Chem. Chem. Phys.* **12**, 5503–5513 (2010).
77. Kresse, G. & Furthmüller, J. Efficient iterative schemes for ab initio total-energy calculations using a plane-wave basis set. *Phys. Rev. B* **54**, 11169–11186 (1996).
78. Kresse, G. & Joubert, D. From ultrasoft pseudopotentials to the projector augmented-wave method. *Phys. Rev. B* **59**, 1758–1775 (1999).
79. Perdew, J. P., Burke, K. & Ernzerhof, M. Generalized Gradient Approximation Made Simple [Phys. Rev. Lett. 77, 3865 (1996)]. *Phys. Rev. Lett.* **78**, 1396–1396 (1997).
80. Grimme, S., Antony, J., Ehrlich, S. & Krieg, H. A consistent and accurate ab initio parametrization of density functional dispersion correction (DFT-D) for the 94 elements H-Pu. *J. Chem. Phys.* **132** (2010).
81. Han, S. et al. Gas-assisted transformation of gold from fcc to the metastable 4H phase. *Nat. Commun.* **11**, 552 (2020).

82. Henkelman, G. & Jónsson, H. Improved tangent estimate in the nudged elastic band method for finding minimum energy paths and saddle points. *J. Chem. Phys.* **113**, 9978–9985 (2000).
83. Zhang, L. & Xia, Z. Mechanisms of oxygen reduction reaction on nitrogen-doped graphene for fuel cells. *J. Phys. Chem. C.* **115**, 11170–11176 (2011).
84. Liu, M. et al. Kinetically favorable edge-type iron–cobalt atomic pair sites synthesized via a silica xerogel approach for efficient bifunctional oxygen electrocatalysis. *J. Mater. Chem. A.* **11**, 708–716 (2023).

Acknowledgements

All authors would like to acknowledge the support from the Ministry of Human Resources and Social Security of China (S20240318), the Natural Science Foundation of Jiangsu Province (BK20210744), Jiangsu Provincial Senior Talent Program (Dengfeng), Guangdong-Macao joint funding program for science and technology innovation (2022A0505020025) and the Young Talent Support Fund from Jiangsu University (Grant No. 5501310023). X.L. and J.Z. are grateful for the support from the Chinese Scholarship Council (CSC); G.-J.X. acknowledges the financial support from NSFC, China (Grant No. 22203041) and Guangdong Basic and Applied Basic Research Foundation, China (Grant No. 2021A1515110406), and Dongguan Key Laboratory of Artificial Intelligence Design for Advanced Materials, China. We also thank the Anhui Absorption Spectroscopy Analysis Instrument Co, Ltd. for in situ XAFS measurements and analysis.

Author contributions

M.L. and J.Z. conceived and designed the experimental ideals. M.L. Z.L., and X.L. synthesized the electrocatalysts. M.L., Z.L., X.L., X.S., L.Z., L.L., J.H., W.Z., and S.S. performed the physical characterization and results discussion. G.X. conducted the theoretical calculations. S.L., T.S., S.W., X.L., G.X., and S.S. analyzed the results. M.L., X.L., G.X., J.Z., and S.S. wrote the manuscript and contributed to the discussion. All the authors commented on the results and approved the final version of the manuscript.

Competing interests

The authors declare no competing interests.

Additional information

Supplementary information The online version contains supplementary material available at https://doi.org/10.1038/s41467-025-65194-0.

Correspondence and requests for materials should be addressed to Xu Li, Guang-Jie Xia, Jianming Zhang or Shuhui Sun.

Peer review information *Nature Communications* thanks Viktoriia Saveleva, Garlef Wartner, and the other, anonymous, reviewer(s) for their contribution to the peer review of this work. A peer review file is available.

Reprints and permissions information is available at http://www.nature.com/reprints

Publisher's note Springer Nature remains neutral with regard to jurisdictional claims in published maps and institutional affiliations.

Open Access This article is licensed under a Creative Commons Attribution-NonCommercial-NoDerivatives 4.0 International License, which permits any non-commercial use, sharing, distribution and reproduction in any medium or format, as long as you give appropriate credit to the original author(s) and the source, provide a link to the Creative Commons licence, and indicate if you modified the licensed material. You do not have permission under this licence to share adapted material derived from this article or parts of it. The images or other third party material in this article are included in the article's Creative Commons licence, unless indicated otherwise in a credit line to the material. If material is not included in the article's Creative Commons licence and your intended use is not permitted by statutory regulation or exceeds the permitted use, you will need to obtain permission directly from the copyright holder. To view a copy of this licence, visit http://creativecommons.org/licenses/by-nc-nd/4.0/.

© The Author(s) 2025